Effect of Aerodynamic Summation on Multirotor UAV Hover Performance Estimates

N. J. Kay*, P. J. Richards, K. A. Stol,
Department of Mechanical and Mechatronics Engineering, University of Auckland, Auckland, New Zealand

R. D. Buchanan,
Cropsy Technologies, Auckland, New Zealand

J. X. J. Bannwarth
Seachange New Zealand Ltd, Auckland, New Zealand

ABSTRACT

Aerodynamic forces are important for the development of multirotor Unmanned Aerial Vehicles, both in selecting hardware and designing controllers. In absence of aerodynamic data specific to a new design, developers turn to summation, adding loads of individual components to represent the whole aircraft. This neglects interaction between the components, a critical aspect for overactuated designs, which often have overlapped or tilted rotors. As such, this work looks at the errors induced by the summation method for a tilted-rotor octorotor. Force estimates from a summation method for steady wind conditions are first compared to a whole-aircraft model and wind tunnel data. Subsequently, the resulting simulated hover performance of each model in elevated winds is compared to wind tunnel free flight tests. Although the summation method tends to underestimate sensitivity to flow angle, it is generally suitable for predicting aircraft performance at lower wind speeds; error increasing with wind speed.

1 INTRODUCTION

Multirotor Unmanned Aerial Vehicles (UAVs) have gained popularity for aerial observation in both military and civilian contexts [1]. The attraction is their ability to operate anywhere without supporting infrastructure [2], and the ability to operate in proximity to obstacles, such as trees and buildings, too hazardous for piloted aircraft [3]. Overactuated aircraft are becoming popular for such operations, due to their enhanced station-holding capabilities while conducting a task [4].

During the development of these aircraft, it is common to employ component summation, adding the individual parts to represent the whole. Product data from off-the-shelf components, such as propellers, motors and batteries, form a database, used in optimisers such as those of Delbecq et al. [5], and Al-Zubaidi and Stol [6]. The net system performance is then estimated from extrapolation of this data. This, however, neglects aerodynamic interaction between components.

Aerodynamic interaction is configuration-dependent and cannot be gauged from databases. For example, when coaxial rotors are employed; the downwash from the upper rotor impinges on the lower rotor, and the inflow from the latter reduces the thrust of the former [7, 8]. Such interaction is also observed with partially-overlapped [9] and canted rotor pairs [4], common on overactuated designs. Interaction with the body also exists, particularly in the aerodynamic moments [10].

Aerodynamic interactions are compounded by wind conditions, which are often highly unsteady in UAV operating environments [11]. The forces on isolated rotors are known to be highly sensitive to wind speed and angle [12]. The forces on the body, and the interaction between rotor wakes, however, are more difficult to predict [13]. While high-fidelity CFD may provide more accurate aerodynamics, this is computationally costly, to the point of being prohibitive, for rapid aircraft development [14]. In absence of such aerodynamic data, the true performance of the aircraft is difficult to predict.

While the summation method is useful for obtaining initial aircraft performance estimates, its accuracy for an overactuated design in its operating environment has not been quantified. This is critical because of the greater component interaction typical of these designs (compared to a conventional quadrotor) and elevated wind environment in which they are intended to be used. This paper looks at the implications of the summation method on the aerodynamics forces acting on an overactuated octorotor, employing a canted-rotor design, and the consequent deviations in simulation-predicted hover performance.

2 METHODOLOGY

2.1 Aircraft

The aircraft for this work is a Canted-Rotor Planar Octorotor, developed by Chen et al. [15, 16]. The layout is shown in Figure 1, with eight rotors canted 31° towards its neighbour, about either the aircraft X (longitudinal) and Y (lateral) axis. There are eight two-blade T-MOTOR 6x2CF propellers (6 in diameter, 2 in pitch, carbon fibre), each driven by a T-MOTOR Navigator MN1806 2300Kv brushless DC motor. The main body has an approximately

* nicholas.kay@auckland.ac.nz

http://www.imavs.org/

http://www.imavs.org/

cylindrical planform, with the rotors at a radius of 0.25 m from the centre of gravity.

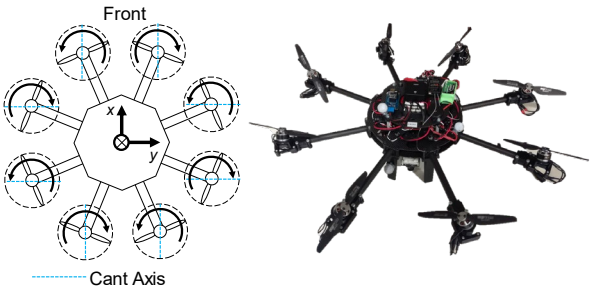

Figure 1: Canted Rotor Planar Octorotor

2.2 Aerodynamic Modelling

Wind tunnel testing was conducted on both the full aircraft (referred to as the "Whole Aircraft" case, with the body and all eight rotors installed), and the individual components (the body and a single rotor, each assessed individually). The test conditions are listed in Table 1. The Angle of Attack (AOA, α) is defined relative to the *X-Y* plane of the body for the Whole-Aircraft and Body-Only cases, and the rotor disk plane for the Rotor-Only test. This can be seen in Figure 2 for the whole-aircraft case. Thus, a negative AOA represents aircraft (or component) nose-down. The rotor speed was maintained as constant for each data collection, with all eight rotors in the whole-aircraft case operating at uniform speed. In all cases, the components were rigidly mounted on a JR3 six-axis loadcell, data being acquired for 30 s at 1000 Hz.

	Whole Aircraft	**Rotor**	**Centre Body**
Wind Speed, *U* (m s $^{-1}$)	0, 4, 6, 8, 10 m s^{-1}		
AOA, α (°)	-60° to +30°, 15° increments		
Rotor Angular Velocity, ω (rad s^{-1})	0, 737, 1317, 1742 (0, 25, 50, 75% maximum)		N/A

Table 1: Experimental conditions for aerodynamic force measurements

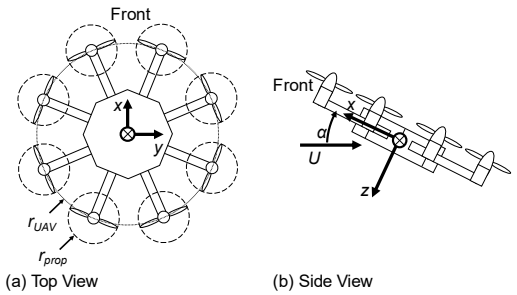

Figure 2: Coordinate System Definition (a) top view and (b) side view

An external, constant-voltage power supply was employed, providing 11.8V at the aircraft. Batteries were, however, fitted to account for their aerodynamics. The effects of blockage, wall interference and downwash impingement are considered negligible due to the size of the wind tunnel section (3.6 m wide, 2.5 m tall) relative to the components tested.

As data could not be acquired for every state likely to be simulated, a semi-empirical model was used to interpolate between the data points. The Bannwarth et al. [17] model was used, due to the ease of fitting experimental data to both the whole aircraft and individual components, as needed for summation.

This model fits curves to experimental data for the *Z*-axis force (F_z), *X*-axis force (F_x) and *Y*-axis moment (M_y) acting on the aircraft, as shown in Equations (1) to (3). The referenced radii are seen in Figure 2. The propeller radius, r_{prop}, is 0.0762 m while that of the airframe, r_{UAV}, is 0.25 m, resulting in circular reference areas A_{prop} of 0.018 m^2 and A_{UAV} of 0.196 m^2. The wind speed and rotor speed are U and ω, respectively, and air density is ρ. The C coefficients are empirically-fitted to the wind tunnel data for the whole-aircraft case, the process of which can be found in Bannwarth et al. [17]. The values used in this work may be found in the Appendix. As seen in the Appendix, these coefficients are dependent upon the Tip-Speed Ratio (TSR, λ) and the AOA. As Bannwarth et al. [17] assumed axisymmetric loading, the *Y*-axis force (F_y) and *X* and *Z* axis moments (M_x and M_z) are neglected. Note that the coefficients are all fitted from whole-aircraft tests, and assume that the n rotors are identical in geometry, speed and inflow angle.

$$F_z = C_{1,z}\frac{1}{2}\rho U^2 A_{UAV} + nC_{2,z}\frac{1}{2}\rho U\omega r_{prop}A_{prop} + nC_{3,z}\frac{1}{2}\rho\omega^2 r_{prop}^2 A_{prop} \quad (1)$$

$$F_x = C_{1,x}\frac{1}{2}\rho U^2 A_{UAV} + nC_{2,x}\frac{1}{2}\rho U\omega r_{prop}A_{prop} \quad (2)$$

$$M_y = C_{M1,y}\frac{1}{2}\rho U^2 A_{UAV} r_{UAV} + nC_{M2,y}\frac{1}{2}\rho U\omega r_{prop}^2 A_{prop} \quad (3)$$

For the summation method, the AOA, TSR and reference areas are unique to each body, with the coordinate frame attached to the individual body. The three C coefficients are then found individually for each component, and forces reconstructed via Equations (4) to (6). Note that r_{UAV} and r_{prop} are exchanged for r_i, and A_{UAV} and A_{prop} are replaced with A_i, where i designates the individual component. These forces and moments must be rotated and translated into the aircraft coordinate frame before being added to the aerodynamic loads of the other components. No models are included for aerodynamic interaction.

$$F_{z,i} = C_{1,z,i}\frac{1}{2}\rho U^2 A_i + C_{2,z,i}\frac{1}{2}\rho U \omega_i r_i A_i + C_{3,z,i}\frac{1}{2}\rho \omega_i^2 r_i^2 A_i \quad (4)$$

$$F_{x,i} = C_{1,x,i}\frac{1}{2}\rho U^2 A_i + C_{2,x,i}\frac{1}{2}\rho U \omega_i r_i A_i \quad (5)$$

$$M_{y,i} = C_{M1,y,i}\frac{1}{2}\rho U^2 A_i r_i + C_{M2,y,i}\frac{1}{2}\rho U \omega_i r_i^2 A_i \quad (6)$$

2.3 Flight Simulation

The flight simulator of Chen et al. [15, 16] was used to assess the effect of summation on hover estimates. The aircraft was given a constant position set-point, which simulated attempting to maintain that position in hover for 700 s. To remove initial simulation transients, the first 100 s of data was discarded prior to analysis. These simulations were run firstly using the whole-aircraft coefficient fits, then the summation method.

Figure 3 shows the basic form of the simulation, which was implemented in Matlab Simulink. This simulation separates the rotor and body aerodynamic loads, in the *Motor Model* and *Body Model* blocks, respectively, allowing for easy implementation of the summation method. It should be noted that the *Motor Model* block not only includes the propeller aerodynamics, but also the inertia of the motor-propeller unit and the electrical characteristics of the motor. Similarly, the *Aircraft Dynamics* block uses the inertia matrix measured on the aircraft as-built, and the *Position and Attitude Control Module* uses the as-built tuning.

For the whole-aircraft simulation, Equations (1) to (3) were implemented across both blocks with the associated whole-aircraft coefficients. However, rather than multiplying the C_2 and C_3 terms by n rotors, the forces for these terms were calculated n times, using the individual rotor speeds. This does not represent a summation model, however, as the coefficients were derived from the whole-aircraft data, thus including interaction, but neglecting local AOA. Simulations using the summation method implemented Equations (4) to (6) in both the *Motor Model* and *Body Model* blocks for each body, using the individual component coefficients found in the Appendix and accounting for the local AOA.

A limitation of the model is its quasi-steady aerodynamics, failing to account for transient delays in the pressure field. Furthermore, the onset flow did not deform over the airframe, as would be expected for flow passing over a body. However, this is consistent across both the summation and whole aircraft simulations.

Various unsteady wind conditions were employed, as listed in Table 2. This turbulent flow was recorded in the wind tunnel with an upstream turbulence grid and then used as an input timeseries of data. At speeds of 0, 5.6 and 12.8 m s^{-1}, Bannwarth [18] performed hover position hold tests with the same wind tunnel configuration and aircraft, providing a reference for the simulation.

Mean Wind Speed, U (m s^{-1})	0, 5.6, 7.4, 9.8, 12.8
Turbulence Intensity, I_u (%)	10

Table 2: Flow Conditions Simulated

3 RESULTS

3.1 Static Load Estimation

Before examining the free-flight performance, the steady force and moment estimates of the baseline model of Bannwarth et al. [17] are compared to the summation form. This is because any errors associated with the data fit carry through to the flight simulation. For the whole-aircraft case, the coefficients are derived from the wind tunnel data, and then the model predictions are found for the same cases. With the summation model, the coefficients were first found for each component from its individual wind tunnel data.

The overall error is summarised in Table 3 as a root-mean-square (RMS) of the error recorded across all cases. The R^2 value for each model is also given as an indication of the overall fit quality of both methods. In all cases, the summation model has greater error than the whole-aircraft case. This is not unexpected, as the whole-aircraft model inherently accounts for aerodynamic interaction between components, unlike the summation method. However, the overall error magnitude is comparable, and may allow for reasonable estimates via summation over portions of the test range.

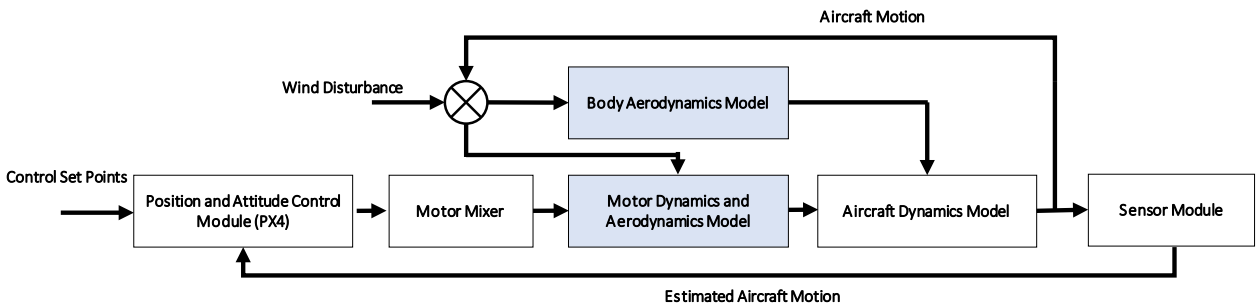

Figure 3: Flight simulation block diagram

http://www.imavs.org/

http://www.imavs.org/

	Whole Aircraft		Summation	
	RMS Error (N, Nm)	R^2	RMS Error (N, Nm)	R^2
F_x	0.45	0.91	0.67	0.80
F_z	0.79	0.99	1.49	0.96
M_y	0.07	0.87	0.11	0.66

Table 3: RMS Error and R^2 for the loads predicted by each model

The greatest change in the absolute RMS error can be seen in F_z, with a 0.70 N increase. The R^2 has a corresponding decline from 0.99 to 0.96 for this case; this is still a high confidence in the fit. This increase in error for the summation method is seen in Figure 4 to be due to a reduced sensitivity to AOA at higher wind speeds. Decomposing F_z into the wind-only and wind-rotor terms in Figure 5 shows that the lack of AOA variability for the summation method is due to the wind-only term. This is clear with a wind speed of 10 m s^{-1}, where the summation curve is flatter than the whole-aircraft model. In contrast, the wind-rotor component of summation aligns with the whole-aircraft model. Note that the rotor-only term is constant for all AOA and wind speeds for both models, hence is not shown in Figure 5.

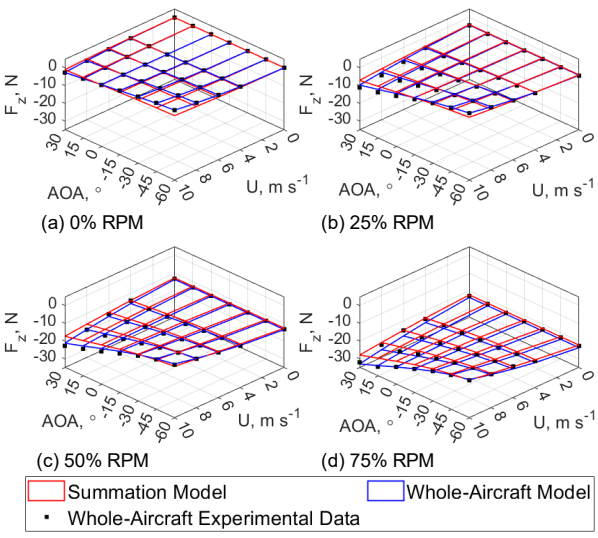

Figure 4: F_z predicted by each model

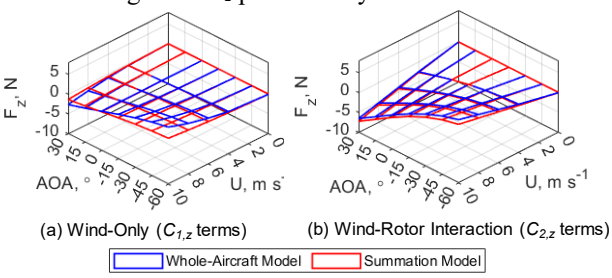

Figure 5: F_z at 75% RPM, decomposed into wind-only and wind-rotor contributions

An increase in the wind-only F_z is expected at non-zero AOA, with a positive force at negative AOA: as the aircraft tilts nose-down, the positive Z-axis rotates towards the mean wind vector, and so a greater portion of F_z is the result of airframe drag. This is seen for the whole-aircraft case, yet not the summation method in Figure 5a. This is surprising, as it would be assumed that F_z is dominated by the large UAV body at high AOA.

In contrast, the wind-rotor terms, on account of rotor sensitivity to inflow conditions, were expected to be more prone to the effects of incident wake from upstream components. However, Figure 5b shows no significant difference in the wind-rotor interaction term between the two methods. Despite these errors, F_z maintains the highest R^2, due to its relatively high force magnitude (the rotors primarily producing thrust in the aircraft Z-axis). Furthermore, the aircraft is unlikely to attain AOA exceeding ±30° in a hover condition. Hence, the differences at high AOA can be mitigated.

In comparison, M_y and F_x have relatively low R^2. This is because of their relatively low mean values, as shown by Figures 6 and 7, respectively. The difference in the whole-method and summation can again be seen to be due to differences in AOA dependence. For M_y, the overall trend is still followed, with a negative AOA producing a negative moment and an increase in both wind and rotor speed increasing the moment.

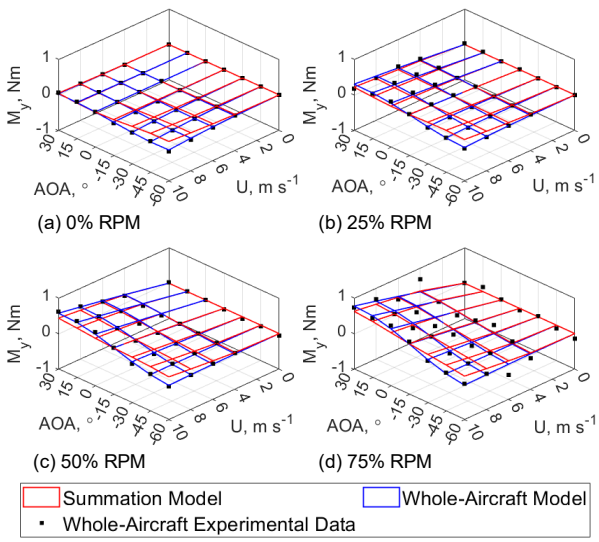

Figure 6: M_y predicted by each model

F_x, on the other hand, shows a difference in the form of the models around 0° AOA. There is a decrease in F_x magnitude at this AOA for the summation method, increasing to a more negative F_x at non-zero AOA until 45° is reached, at which point the magnitude decreases again. In contrast, the whole-aircraft model shows a gradually more positive F_x for any deviation from 0° AOA. Interestingly, the wind tunnel data shows both

http://www.imavs.org/

behaviours, with the 0° local minimum more evident at higher rotor speeds, suggesting neither model is particularly favourable in this case.

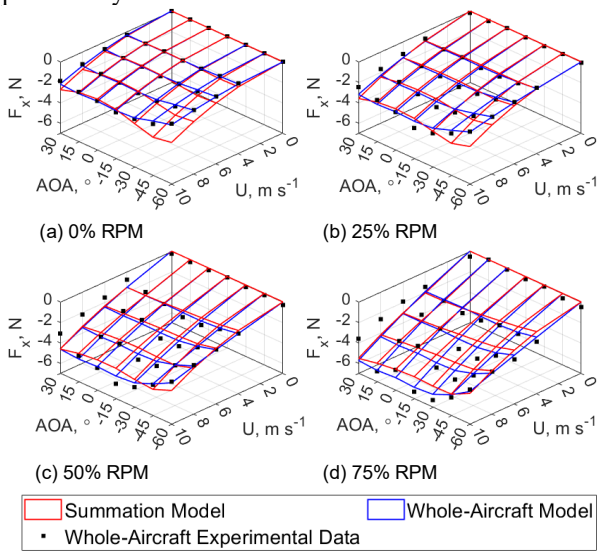

Figure 7: F_x predicted by each model

Figure 8 shows that not only do the models differ in form, but so does the experimental data for F_x from the wind tunnel, seen as black dots in each sub-plot. For the body-only test, no propellers were installed, while the whole-aircraft C_1 terms the propellers were installed, but unpowered. The propellers were free to windmill, representing the only physical difference in the two experimental data sets. A minimum F_x magnitude at 0° is expected, as this is when the aircraft is presenting minimal frontal area, hence minimum drag is expected. Deviating from this increases the projected area, and so drag, until the rotation of the X-axis away from the wind vector reduces the influence of drag on F_x. This is the behaviour seen in the body-only case, both in the model and the experimental data, but not so for the whole-aircraft. While this difference results in the whole-aircraft model being more representative at low rotor speeds, it is unlikely that the aircraft will operate with the rotors unpowered in hover. At higher rotor speeds, neither method captures the exact form of F_x,

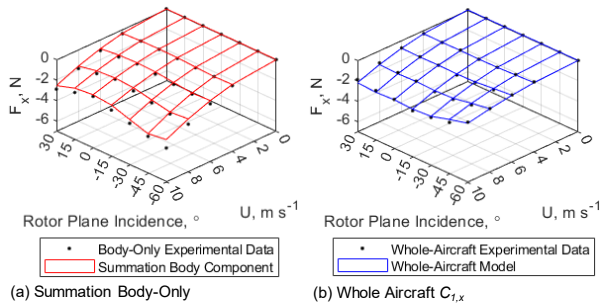

Figure 8: Fit of (a) the body-only F_x and (b) the whole-aircraft wind-only component F_x to wind tunnel data

Overall, the summation model captures the trends of F_z and M_y, but displays increasing error at high AOA. This suggests that the summation method may not be viable with higher wind speeds, where greater AOA are required, but may be appropriate at low wind speeds.

3.2 Station-Keeping Simulation

Using the coefficient fits obtained from the wind tunnel testing, Figure 9 shows the RMS position error, in millimetres, for both simulation with the whole-aircraft and summation methods. Additionally, the wind tunnel flight test data can be seen for mean wind speeds of 0, 5.6 and 12.8 m s^{-1}. Both models underestimate the position error in the no-wind condition, by an order of magnitude, with little difference between the models. Indeed, the wind tunnel flight test unexpectedly shows a higher position error for the no-wind case than with a wind speed of 5.6 m s^{-1}. This is likely due to the aircraft operating in its recirculated wake: as the wind tunnel has a closed-wall test section, in still air the wake from the rotors deflects off the floor and walls and back on to the aircraft. As the mean wind speed increases, this unsteady wake is convected downstream, reducing its impact on the aircraft. As the simulation does not suffer from wall effects, the expected deviation is much lower than the wind tunnel test without wind. Hence, this difference is likely due to experimental conditions.

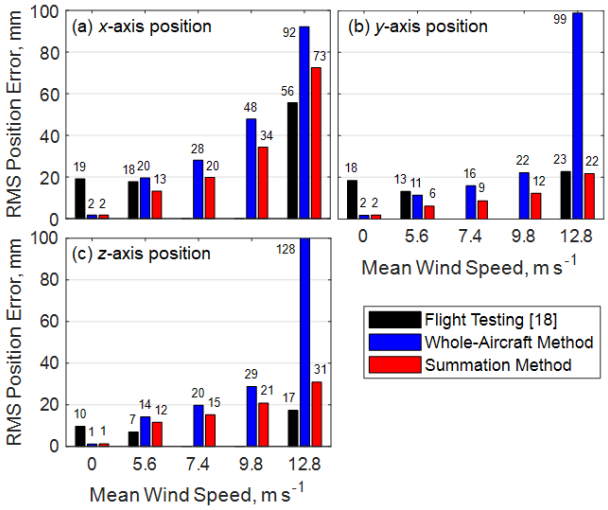

Figure 9: RMS Position Error for each model

Increasing the wind speed produces an increase in the position error predicted by both simulation methods. This is to be expected, due to the increased onset turbulent wind disturbance, and aligns with the experimental data. However, the predicted error for the simulations, particularly the whole-aircraft method, exceeds that of the flight test, most notably at 12.8 m s^{-1}. This is likely due to two critical assumptions of the simulation: quasi-steady response and uniform flow across the entire

http://www.imavs.org/

airframe. In reality, the flow is not uniform across the airframe due to the irregular, chaotic nature of turbulence, in addition to flow deformation due to the aircraft. This, in turn, reduces the net variation in load on the aircraft [19].

While these inaccuracies are inherent to the simulation, the greater position error for the whole-aircraft model highlights a difference in modelling methods. Interestingly, this places the summation method more in alignment with the experimental data. Although interference effects are expected to be better handled through the whole-aircraft model, the latter may also produce excessively-variable rotor speeds to produce a desired force. This is because the local AOA at each rotor was not considered during the coefficient fits. As such, the whole-aircraft model cannot accurately predict the contribution from each rotor when they are no longer run at a uniform speed. In contrast, the summation model is based on the individual rotor AOA.

To investigate this further, Figure 10 shows a sample of the predicted aircraft forces for $U = 12.8$ m s^{-1}. It should be noted that the incident flow is identical at a given timestep for the two cases. The signal for the whole-aircraft method (on left) is considerably noisier than that of the summation method (on right).

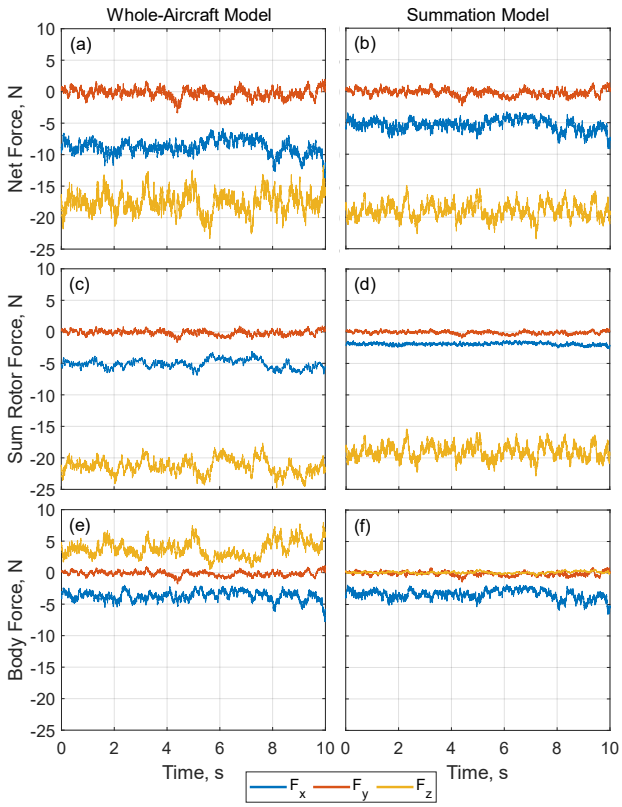

Figure 10: Simulation force estimates for (left) Whole-Aircraft Model and (right) Summation Model when U = 12.8 m s-1 for (a-b) the net aircraft, (c-d) the total rotor force and (e-f) the body contribution

The greater variation in the whole-aircraft model is to be expected, given the greater AOA sensitivity seen in the former combined with the quasi-steady assumption. The body-only force is the primary indicator of this, as the rotor-only and net aircraft estimates are altered by the commanded inputs. Not only does F_z for the body show considerably more variation, but also that its magnitude is greater. In the summation method, F_z is near-zero throughout the period shown, while the whole aircraft model produces +5 N. While this may be due to the increased AOA sensitivity, a higher drag estimate may also result in a greater nose-down attitude. More thrust needed to offset the higher drag, thus increasing F_z as the axis rotates towards the drag vector. As such force components cannot be measured from the free-flight test, this cannot be directly validated against experiments.

However, the pitch angle may be used to gauge drag estimates. As the horizontal thrust capability was not employed during the free flight tests in the wind tunnel, the aircraft must tilt to resist drag. Figure 11 shows the pitch angle of the aircraft in flight and in the simulations.

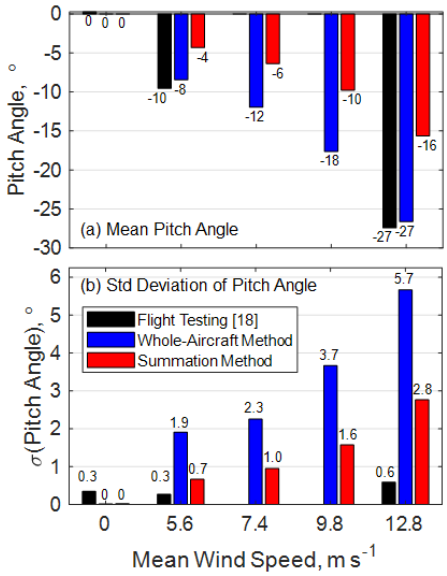

Figure 11: Mean and standard deviation of the Pitch Angle for each model compared with wind tunnel data

With its better fit to the steady-state aerodynamic loads, particularly M_y and F_x in this case, the whole-aircraft model produces a similar mean pitch angle to the free-flight data. The summation model, which was less sensitive to AoA and predicted lower forces, produces a lesser mean pitch. This suggests that the force estimates of the whole-aircraft model are, on average, nearer the expected. This underestimation of the pitch angle for the summation method is important as it could result in an aircraft being built with insufficient pitch authority. Furthermore, in roles requiring precision, such as object interaction or photography, the increased pitch angle experienced in

http://www.imavs.org/

flight compared to the model would result in greater positional error for the end effector.

The transient pitch angle ranges for both models are exacerbated by the quasi-steady assumption, and greatly exceed the wind tunnel range. With its greater AOA sensitivity, the whole-aircraft model experiences a greater pitch angle range than its summation counterpart. This excessive motion may lead to excessively aggressive tuning during controller development.

4 DISCUSSION

The major limitation of this work is the reliance on data for a single aircraft. Although this means that the trends cannot be quantified for all configurations, it does nonetheless provide an insight into the issues with summation. For example, all axes show an increase in error when using the summation method to generate force estimates, compared to a model based on the whole aircraft. This is inevitable, as the former has no means of accounting for component interaction. As such, aircraft with considerable rotor-airframe overlap can be expected to deviate further from the true state when using summation methods. The question, however, is the viability of summation for initial aircraft performance estimates, rather than high-fidelity simulation.

The lack of AOA sensitivity, in particular, could lead to issues when using the summation method. This is mainly through the risk of underestimating pitch authority requirements in higher wind speeds. Caprace et al. [10] noted that rotor-frame interaction contributed significantly to the pitch moment. As such, summation is more suited for low-speed environments, with the whole-aircraft model more appropriate for higher flow speeds. However, this would require prototype tests or high-fidelity simulation data to perform the necessary fits. However, such accuracy comes at a cost: Caprace et al. [10] used 420 CPU hours per rear rotor revolution for their vortex method to account for rotor interaction. In contrast, the simulation employed here required fewer than 150 CPU seconds for the full 700 second flight. Although this low solving cost applies to both the whole-aircraft and summation methods, the input data for the latter is much more accessible through data sheets and low-order models. As such, at low wind speeds, summation is a valuable tool for rapid development.

A limitation which may not be as avoidable at low wind speeds is overlapped rotors. Although canted rotors do interact with each other, this is not to the extent of fully-coaxial or directly overlapping designs. This means that novel configurations, such as that proposed by Al-Zubaidi and Stol [6], would not lend themselves to a simple summation, as the rotors are always, and significantly, interacting in all phases of flight. At minimum, a thrust reduction model would be needed for the coaxial pair. It may be suitable to use a simple BEMT-based thrust deficit, but this would require testing of such an aircraft for validation.

4. CONCLUSIONS

The aerodynamic loads acting on an octorotor have been assessed via a modified empirical aerodynamic model, estimating the loads acting on a multirotor aircraft as the sum of the loads on individual components. Despite neglecting interaction effects, for a quasi-planar airframe configuration, this model produces steady force estimates comparable to that of the whole-aircraft case, albeit with increasing error at high wind speeds. Flight simulations, however, showed that the unsteady response is much less than for a whole-aircraft equivalent, with the mean pitch angle also differing from the wind tunnel expectations. Despite this, the summation method provides a reasonable estimate of the aerodynamic loads at wind speeds below 10 m s^{-1} and may prove valuable for initial development of an aircraft against the criteria of hover performance.

ACKNOWLEDGEMENTS

The research reported in this article was conducted as part of “Enabling unmanned aerial vehicles (drones) to use tools in complex dynamic environments UOCX2104”, which is funded by the New Zealand Ministry of Business, Innovation and Employment.

REFERENCES

[1] J. Walker, "Industrial Uses of Drones—5 Current Business Applications," ed: TechEmergence, 2017.

[2] R. Austin, *Unmanned aircraft systems: UAVS design, development, and deployment*, 1 ed. (no. Book, Whole). West Sussex, UK: John Wiley & Sons, 2010.

[3] ICAO, "ICAO Cir 328 Unmanned Aerial Systems (UAS)," in "Circular," Montreal, Canada, 2011. [Online]. Available: https://www.icao.int/meetings/uas/documents/circular%20328_en.pdf

[4] P. J. Richards, K. A. Stol, J. Basra, T. F. Walker, J. X. J. Bannwarth, and Z. J. Chen, "Station Keeping of Multi-Rotor UAVs in Windy Conditions," presented at the 19th Australasian Wind Engineering Society Workshop, Torquay, Vic, Australia, April 4-6, 2018.

[5] S. Delbecq, M. Budinger, A. Ochotorena, A. Reysset, and F. Defaÿ, "Efficient sizing and optimization of multirotor drones based on scaling laws and similarity models," *Aerospace Science and Technology,* vol. 102, p. 105873, 2020.

[6] S. Al-Zubaidi and K. A. Stol, "Preliminary design optimisation of a novel fixed-tilt heterogeneous UAV for horizontal agility," in *2022 International*

http://www.imavs.org/

Conference on Unmanned Aircraft Systems (ICUAS), 2022: IEEE, pp. 1489-1496.

[7] H. Zhu, H. Nie, L. Zhang, X. Wei, and M. Zhang, "Design and assessment of octocopter drones with improved aerodynamic efficiency and performance," *Aerospace Science and Technology,* vol. 106, p. 106206, 2020.

[8] M. Brazinskas, S. D. Prior, and J. P. Scanlan, "An empirical study of overlapping rotor interference for a small unmanned aircraft propulsion system," *Aerospace,* vol. 3, no. 4, p. 32, 2016.

[9] B. Theys, G. Dimitriadis, P. Hendrick, and J. De Schutter, "Influence of propeller configuration on propulsion system efficiency of multi-rotor Unmanned Aerial Vehicles," in *2016 international conference on unmanned aircraft systems (ICUAS)*, 2016: IEEE, pp. 195-201.

[10] D.-G. Caprace, A. Ning, P. Chatelain, and G. Winckelmans, "Effects of rotor-airframe interaction on the aeromechanics and wake of a quadcopter in forward flight," *Aerospace Science and Technology,* vol. 130, p. 107899, 2022.

[11] S. Watkins, J. Milbank, B. J. Loxton, and W. H. Melbourne, "Atmospheric winds and their implications for Micro Air Vehicles," *AIAA Journal,* vol. 44, no. 11, pp. 2591-2600, 2006, doi: https://doi.org/10.2514/1.22670.

[12] M. Cerny and C. Breitsamter, "Investigation of small-scale propellers under non-axial inflow conditions," *Aerospace Science and Technology,* vol. 106, p. 106048, 2020.

[13] C. Rodríguez de Cos and J. Á. Acosta, "Explicit aerodynamic model characterization of a multirotor unmanned aerial vehicle in quasi-steady flight," *Journal of Computational and Nonlinear Dynamics,* vol. 15, no. 8, p. 081005, 2020.

[14] M. C. Ruiz, M. Scanavino, D. D'Ambrosio, G. Guglieri, and A. Vilardi, "Experimental and numerical analysis of hovering multicopter performance in low-Reynolds number conditions," *Aerospace Science and Technology,* vol. 128, p. 107777, 2022.

[15] Z. Chen, K. Stol, and P. Richards, "Preliminary design of multirotor UAVs with tilted-rotors for improved disturbance rejection capability," *Aerospace Science and Technology,* vol. 92, pp. 635-643, 2019.

[16] Z. J. Chen, J. X. Bannwarth, K. A. Stol, and P. J. Richards, "Analysis of a Multirotor UAV with Tilted-rotors for the Purposes of Disturbance Rejection," in *2018 International Conference on Unmanned Aircraft Systems (ICUAS)*, 2018: IEEE, pp. 864-873.

[17] J. X. J. Bannwarth, Z. J. Chen, K. A. Stol, B. A. MacDonald, and P. J. Richards, "Aerodynamic Force Modeling of Multirotor Unmanned Aerial Vehicles," *AIAA Journal,* vol. 57, no. 3, pp. 1250-1259, 2019, doi: 10.2514/1.J057165.

[18] J. X. J. Bannwarth, "Aerodynamic Modelling and Wind Disturbance Rejection of Multirotor Unmanned Aerial Vehicles," PhD, Department of Mechanical Engineering, The University of Auckland, Auckland, New Zealand, 2022.

[19] I. Andreu-Angulo, H. Babinsky, H. Biler, G. Sedky, and A. R. Jones, "Effect of Transverse Gust Velocity Profiles," *AIAA Journal,* vol. 59, no. 1, pp. 1-11, 2020, doi: https://doi.org/10.2514/1.j059678.

APPENDIX A: COEFFICIENT FITS

Whole-Aircraft
$C_{1,x} = -0.2003\cos(\alpha) + 0.0060\cos(3\alpha) + 0.0102\cos(7\alpha)$
$C_{2,x} = -0.0396\left(1 - e^{-0.1584\lambda}\right)\cos(\alpha) + 0.0086\left(1 - e^{-0.0565\lambda}\right)\cos(3\alpha)$
$C_{1,z} = -0.4326\sin(\alpha) - 0.0055$
$C_{2,z} = -0.0815\sin(\alpha) + 0.4583\left(1 - e^{-9.31\times10^{-4}\lambda}\right)\sin(3\alpha) - 0.0175$
$C_{3,z} = -0.0152$
$C_{M1,y} = -0.0150\cos(\alpha) + 0.0126\cos(3\alpha) + 0.0271\sin(2\alpha)$
$C_{M2,y} = 0.0549\left(1 - e^{-0.5307\lambda}\right)\cos(\alpha) + 0.2729\left(1 - e^{-0.1174\lambda}\right)\sin(2\alpha)$
Rotor-Only
$C_{1,x} = -0.0076\cos(\alpha) - 0.0055\cos(3\alpha) + 0.0055\cos(7\alpha)$
$C_{2,x} = -0.0330\left(1 - e^{-0.0349\lambda}\right)\cos(\alpha) - 0.0031\left(1 - e^{-0.0735\lambda}\right)\cos(3\alpha)$
$C_{1,z} = -0.1124\sin(\alpha) + 0.0025$
$C_{2,z} = -0.1039\sin(\alpha) + 2.192\left(1 - e^{-5.18\times10^{-4}\lambda}\right)\sin(3\alpha) - 0.0308$
$C_{3,z} = -0.0149$
$C_{M1,y} = 0.0232\cos(\alpha) - 0.0140\cos(3\alpha) + 0.0236\sin(2\alpha)$
$C_{M2,y} = 0.0652\left(1 - e^{-0.0632\lambda}\right)\cos(\alpha) + 0.0630\left(1 - e^{-0.0278\lambda}\right)\sin(2\alpha)$
Body-Only
$C_{1,x} = -0.2524\cos(\alpha) + 0.1095\cos(3\alpha) - 0.0062\cos(7\alpha)$
$C_{1,z} = -0.0845\sin(\alpha) - 0.0192$
$C_{M1,y} = 0.0103\cos(\alpha) - 0.0227\cos(3\alpha) - 0.0058\sin(2\alpha)$

Table 4: Coefficient Fits for Each Model